

# Manipulating Band Structure through Reconstruction of Binary Metal Sulfide for High-Performance Thermoelectrics in Solution-Synthesized Nanostructured $\text{Bi}_{13}\text{S}_{18}\text{I}_2$

Biao Xu<sup>+</sup>, Tianli Feng<sup>+</sup>, Matthias T. Agne, Qing Tan, Zhe Li, Kazuki Imasato, Lin Zhou, Je-Hyeong Bahk, Xiulin Ruan, G. Jeffery Snyder, and Yue Wu\*

**Abstract:** Reconstructing canonical binary compounds by inserting a third agent can significantly modify their electronic and phonon structures. Therefore, it has inspired the semiconductor communities in various fields. Introducing this paradigm will potentially revolutionize thermoelectrics as well. Using a solution synthesis,  $\text{Bi}_2\text{S}_3$  was rebuilt by adding disordered Bi and weakly bonded I. These new structural motifs and the altered crystal symmetry induce prominent changes in electrical and thermal transport, resulting in a great enhancement of the figure of merit. The as-obtained nanostructured  $\text{Bi}_{13}\text{S}_{18}\text{I}_2$  is the first non-toxic, cost-efficient, and solution-processable n-type material with  $zT = 1.0$ .

**T**hermoelectrics, in which the waste heat can be converted into electricity in a silent and reliable way, have gained renewed interests.<sup>[1]</sup> The semiconductor industry, of which thermoelectrics is a subset, has been primarily relying on binary compounds. Specifically, the state-of-the-art thermoelectric compounds are  $\text{Bi}_2\text{Te}_3$ <sup>[2]</sup> operating at low-temperature (300–500 K) and  $\text{PbTe}$ ,<sup>[3]</sup>  $\text{SnSe}$ ,<sup>[4]</sup> and  $\text{CoSb}_3$ <sup>[5]</sup> at medium

temperature (500–900 K). The conversion efficiency of thermoelectrics is evaluated by the figure of merit,  $zT = S^2\sigma T/\kappa$ . Typical ways to enhance the  $zT$  of these binary compounds include increasing the power factor,  $S^2\sigma$ , through band engineering, such as energy filtering,<sup>[6]</sup> resonant level,<sup>[7]</sup> and/or diminishing  $\kappa$  via structural engineering, as exemplified by the atomic-level defect<sup>[8]</sup> nanoscale grain boundary.<sup>[9]</sup>

Aside from performance, cost and toxicity also raise critical concerns. Since Co and Pb are toxic and Te is also scarce (0.001 ppm in earth crust), the earth-abundant (500 ppm) and eco-friendly sulfur-based counterparts have attracted attentions as potential alternatives.<sup>[10]</sup> However, their performance is impaired by lower carrier mobility ( $\mu$ ) owing to the more ionic bonding and higher  $\kappa$  ascribed to the lower atomic weight. The commonly used strategies to improve  $zT$  have encountered a bottleneck to achieve  $zT = 1.0$  in binary metal sulfides, especially for the n-type leg.

Recently, dismantling and reconstructing the canonical binary compound by inserting a third agent<sup>[11]</sup> has inspired material explorations in various fields, such as electronic devices ( $\text{SnS}_2\text{-(N}_2\text{H}_5)_4\text{Sn}_2\text{S}_6$ )<sup>[12]</sup> and radiation detectors ( $\text{HgS-Cs}_2\text{Hg}_6\text{S}_7$ ).<sup>[13]</sup> This strategy may also reconstruct the crystal structure of binary thermoelectric compounds, resulting in possible modifications of electronic and phonon structures. However, it has seldom been attempted, which is probably due to the synthetic complexity and the sophisticated interplay between the transport properties<sup>[1]</sup> ( $S$ ,  $\sigma$ , and  $\kappa$ ). Herein, we chose the n-type binary metal sulfide,  $\text{Bi}_2\text{S}_3$  and inserted a third environmentally compatible and earth-abundant element, iodine. The resultant  $\text{Bi}_{13}\text{S}_{18}\text{I}_2$  has the crystal symmetry changed and several novel structural motifs introduced, leading to substantially modified electronic and phonon structures. Consequently, it significantly outperformed the parent compound ( $\text{Bi}_2\text{S}_3$ ). The high  $zT$  (1.0 at 788 K), as well as eco-friendly and cost-efficient constituent elements qualify this material as a competitive alternative to conventional Te-based thermoelectrics.

$\text{Bi}_{13}\text{S}_{18}\text{I}_2$  has a complex crystal structure that belongs to a trigonal lattice with the space group  $P3$ .<sup>[14]</sup> There are four sites for disordered Bi(X), each with a  $1/4$  occupancy. These disordered Bi(X) atoms at the  $(1/3, 2/3, z)$  sites coordinate with six S atoms to form a wheel-like cluster (Figure 1 a). The Bi(X) atom disorder and Bi–Bi bonding had been validated through both single-crystal and powder X-ray diffraction in previous studies.<sup>[14]</sup> This unusual Bi–Bi bond had also been witnessed in  $\text{CsBi}_4\text{Te}_6$ <sup>[15]</sup> and  $\text{BiTe}$ .<sup>[16]</sup> Between the disordered Bi(X) atoms, the  $\text{Bi}_4\text{S}_6$  clusters serve as the connecting arms

[\*] Prof. Dr. B. Xu,<sup>[1]</sup> Z. Li, Prof. Dr. Y. Wu  
Department of Chemical and Biological Engineering  
Iowa State University, Ames, IA 50011 (USA)  
E-mail: yuewu@iastate.edu

Prof. Dr. B. Xu<sup>[1]</sup>  
College of Chemical Engineering  
Nanjing University of Science and Technology  
Nanjing, Jiangsu 210094 (China)

Dr. T. Feng,<sup>[1]</sup> Prof. Dr. X. Ruan  
Department of Mechanical Engineering, Purdue University  
West Lafayette, IN 47907 (USA)

M. T. Agne, K. Imasato, Prof. Dr. G. J. Snyder  
Department of Materials Science and Engineering  
Northwestern University, Evanston, IL 60208 (USA)

Dr. Q. Tan  
State Key Laboratory for Advanced Metals and Materials  
University of Science and Technology Beijing  
Beijing 100083 (China)

Prof. Dr. L. Zhou  
Ames Laboratory, Department of Energy, Ames, IA 50011 (USA)

Prof. Dr. J. H. Bahk  
Department of Mechanical and Materials Engineering  
University of Cincinnati, Cincinnati, OH 45221 (USA)

[†] These authors contributed equally to this work.

Supporting information and the ORCID identification number(s) for the author(s) of this article can be found under:  
<https://doi.org/10.1002/anie.201713223>.

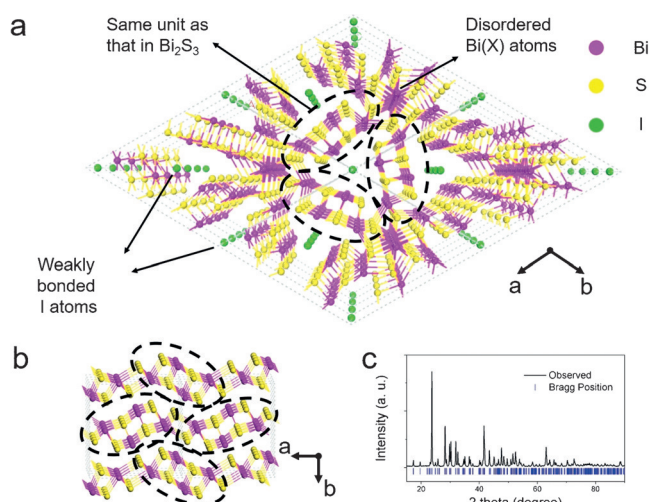


**Figure 1.** The crystal structure of a)  $\text{Bi}_{13}\text{S}_{18}\text{I}_2$  vs. b)  $\text{Bi}_2\text{S}_3$ . The dashed circles illustrate the inherited fragment in  $\text{Bi}_{13}\text{S}_{18}\text{I}_2$  from  $\text{Bi}_2\text{S}_3$ . c) The powder X-ray diffraction (PXRD) profile of the bulk  $\text{Bi}_{13}\text{S}_{18}\text{I}_2$ .

(Figure 1a). The Bi–S coordination styles in these clusters (Figure 1a, circled region) are almost the same with those in  $\text{Bi}_2\text{S}_3$  (Figure 1b, circled region). These Bi and S atoms construct a 3D framework and create two one-dimensional tunnels propagating along the [001] axis in each unit cell, inside which the I atoms reside. It is noteworthy that the distance between iodine and the nearest atom (Bi) is around 3.57 Å, which is much longer than the sum (2.79 Å) of the covalent radii of Bi (1.46 Å) and I (1.33 Å). This is reminiscent of open framework compounds as exemplified by clathrate ( $\text{Ba}_8\text{Ga}_{16}\text{Ge}_{30}$ )<sup>[17]</sup> or CoSb<sub>3</sub>-based skutterudite.<sup>[5]</sup> The addition of disordered Bi sites, Bi–Bi bonds, and the iodine sublattice going from  $\text{Bi}_2\text{S}_3$  to  $\text{Bi}_{13}\text{S}_{18}\text{I}_2$  are likely to alter its electronic and thermal properties.

Bulk polycrystalline samples of  $\text{Bi}_{13}\text{S}_{18}\text{I}_2$  (6.70 g cm<sup>-3</sup>, relative density: 96.4%) could be prepared from spark plasma sintering (SPS) commercial  $\text{Bi}_2\text{S}_3$  and  $\text{BiI}_3$  (the molar ratio is 5.60:1) at 600 °C. We have conducted an analysis of the powder X-ray diffraction (PXRD) profile of the bulk  $\text{Bi}_{13}\text{S}_{18}\text{I}_2$  and confirmed this single-phase product (Figure 1c). The Rietveld refinement was also carried out (Supporting Information, Table S1 and Figure S2). Energy dispersive spectrum (EDS) detected the chemical composition (measured at. %: Bi 40.1, S 53.6, I 6.3, theoretical at. % of  $\text{Bi}_{13}\text{S}_{18}\text{I}_2$ : Bi 39.3, S 54.5, I 6.1).

Along with the bulk  $\text{Bi}_{13}\text{S}_{18}\text{I}_2$  prepared, we have also adopted a solution-phase method to synthesize the nanocrystalline counterpart, which was then unequivocally characterized by various techniques. First, the PXRD pattern agreed well with the simulated one (Supporting Information, Figure S6). Furthermore, EDS confirmed the chemical composition (at. %: Bi 39.0, S 55.0, I 6.0, theoretical at. %: Bi 39.3, S 54.5, I 6.1). Finally, transmission electron microscopy (TEM) depicted the microstructure of the product. As expected from the trigonal crystal structure of  $\text{Bi}_{13}\text{S}_{18}\text{I}_2$ , an anisotropic rod-like shape could be found (Figure 2a). The axial direction of the nanorod was indexed as [001] by high-

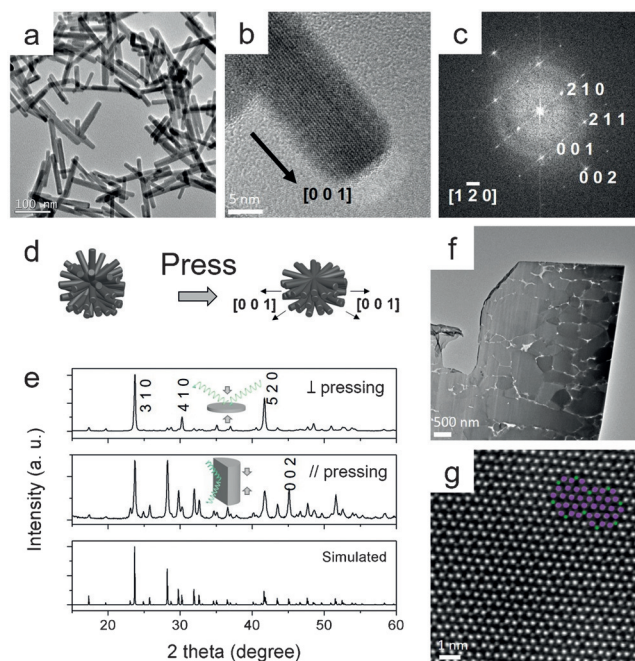


**Figure 2.** a) Low-magnification and b) high-resolution TEM images of  $\text{Bi}_{13}\text{S}_{18}\text{I}_2$  nanorods, c) fast Fourier transform pattern, d) illustration of the spark plasma sintering process that induced the crystallographic anisotropy, e) PXRD patterns of the as-sintered nanostructured material along different directions and the simulated pattern, f) TEM image of a focused-ion-beam-cut thin section of the as-sintered nano  $\text{Bi}_{13}\text{S}_{18}\text{I}_2$ , g) HAADF-STEM image of an as-sintered nano  $\text{Bi}_{13}\text{S}_{18}\text{I}_2$ , showing the hexagonal periodicity of I atoms as darker dots (green spheres) and Bi atoms as brighter dots (purple spheres).

resolution transmission electron microscopy (HRTEM, Figure 2b,c).

The scalable (9.0 g per batch) synthesis of  $\text{Bi}_{13}\text{S}_{18}\text{I}_2$  nanopowder enabled us to consolidate it into a macroscopic cylinder (diameter 10 mm × height 12 mm, 6.33 g cm<sup>-3</sup> relative density = 91.1%). After SPS, the crystal phase was preserved according to PXRD (Figure 2e). From the TEM (Figure 2f) of the focused-ion-beam (FIB)-cut nanosample, the grain size was estimated to be 800 ± 300 nm. EDS corroborated the nearly identical atomic percentages of Bi, S, and I (at. %: Bi 39.4, S 54.3, I 6.3) to nominal values (at. %: Bi 39.3, S 54.5, I 6.1). HRTEM clearly revealed the lattice fringe of (100), (001) plane and honeycomb-like pattern along [001] axis (Supporting Information, Figure S7). The atomically resolved high-angle annular dark-field scanning transmission electron microscopy (HAADF-STEM) image taken along [001] zone axis was in good accordance with the atomic model (Figure 2g).  $\text{BiCl}_3$  was mixed with the  $\text{Bi}_{13}\text{S}_{18}\text{I}_2$  nanopowder (Supporting Information, Figure S8c–f) and then SPSed to study the dopant effect.

Interestingly, the as-compressed nanostructured material manifested a strong crystallographic anisotropy (Figure 2e). In the cross-plane (⊥ pressing) XRD, (hk0) reflection peaks, such as (310), (410) and (520), were notably enhanced. In stark contrast, in the in-plane (∥ pressing) XRD, (002) peak was relatively much stronger. This anisotropy might stem from the anisotropic grain structure of the starting crystallite

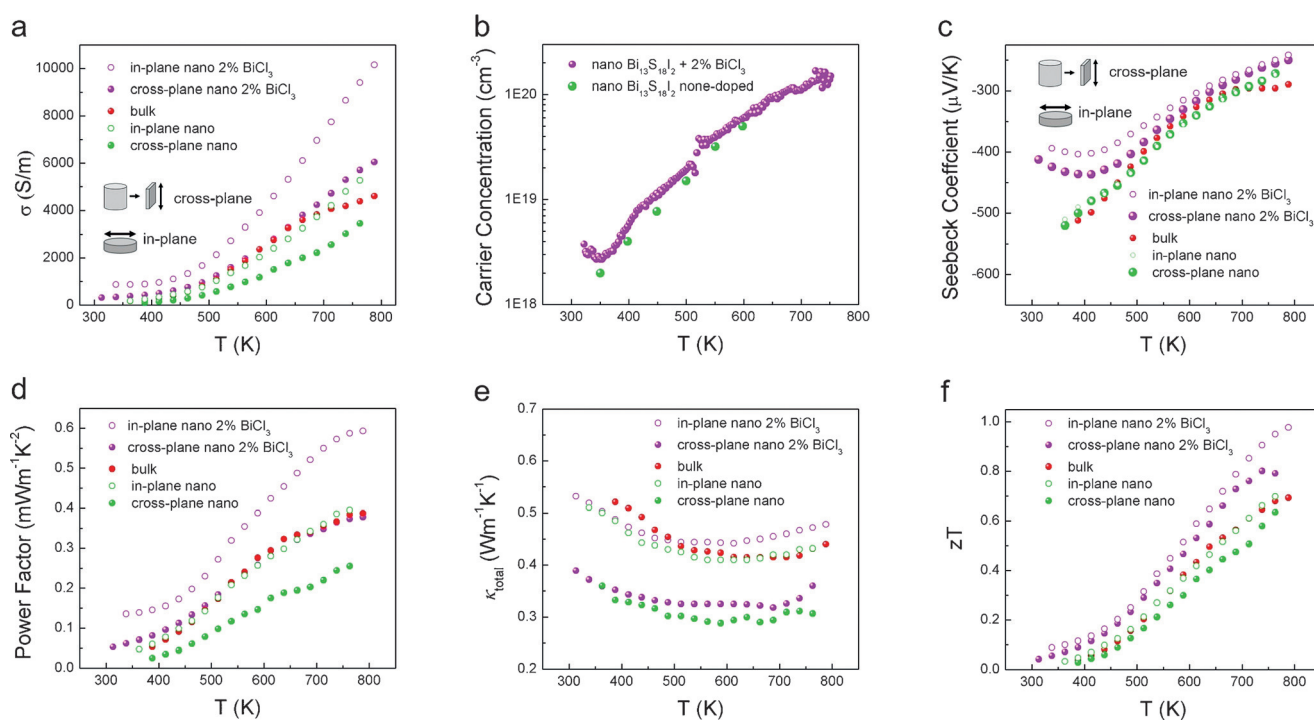


**Figure 3.** Temperature dependence of a) electrical conductivity, b) Hall carrier concentration, c) Seebeck coefficient, d) power factor, e) total thermal conductivity, f) Figure of merit,  $zT$ , of the three  $\text{Bi}_{13}\text{S}_{18}\text{I}_2$  samples: “bulk”, “nano” (no  $\text{BiCl}_3$  added), and “nano with 2%  $\text{BiCl}_3$ ”.

of nanorods as the long axis ([001] direction) of the nanorod tended to lie perpendicular to the pressing direction (Figure 2d). Contrarily, for the bulk polycrystalline sample of  $\text{Bi}_{13}\text{S}_{18}\text{I}_2$  that was synthesized via sintering randomly oriented  $\text{Bi}_2\text{S}_3$  and  $\text{BiI}_3$  powder, almost no anisotropy was observed (Supporting Information, Figure S2).

Having successfully synthesized and characterized both bulk and nano  $\text{Bi}_{13}\text{S}_{18}\text{I}_2$  samples on a large scale, we studied their thermoelectric properties (Figure 3). First, the electrical conductivities ( $\sigma$ ) of the so-called bulk  $\text{Bi}_{13}\text{S}_{18}\text{I}_2$ , nano  $\text{Bi}_{13}\text{S}_{18}\text{I}_2$ , and nano  $\text{Bi}_{13}\text{S}_{18}\text{I}_2 + 2\%$   $\text{BiCl}_3$  samples all increased with ascending temperature, 313–788 K (Figure 3a). This was indicative of a semiconductor-like transport behavior. Nearly no anisotropy was found in  $\sigma$  of the bulk  $\text{Bi}_{13}\text{S}_{18}\text{I}_2$  sample due to the random grain orientation (Supporting Information, Figure S5e–h). Contrarily,  $\sigma$  showed pronounced differences in two directions of the nanosamples (Figure 3a).  $\sigma$  of the undoped nanosample was similar with that of the bulk sample, while doping had induced a significant enhancement of  $\sigma$  in the nano  $\text{Bi}_{13}\text{S}_{18}\text{I}_2 + 2\%$   $\text{BiCl}_3$  sample (Figure 3a). The carrier concentration ( $n_{\text{H}}$ ) of undoped nanosample showed a steady increase as temperature rose (Figure 3b). This again corroborated the semiconductor-like characteristics. Upon doping of  $\text{BiCl}_3$ ,  $n_{\text{H}}$  was higher than that of the undoped nanosample over the whole temperature range (Figure 3b; Supporting Information, Table S2).

The Seebeck coefficients ( $S$ , Figure 3c) of all the samples had negative signs throughout the temperatures of interest, indicating that electron was the majority carrier. The nano and bulk undoped samples exhibited quite similar Seebeck coefficients (Figure 3c), implying their nearly identical carrier concentration. On the other hand, the lower magnitude of

Seebeck coefficient of the  $\text{BiCl}_3$ -doped nanosample (Figure 3c; Supporting Information, Figure S10) compared to the undoped nanosample might be attributed to its higher carrier concentration (Figure 3b). The power factor was then calculated as  $S^2\sigma$  (Figure 3d). The  $\text{BiCl}_3$ -doped sample exhibited a much larger (ca. 2 times) power factor compared with the undoped sample. The highest power factor attained in the nano  $\text{Bi}_{13}\text{S}_{18}\text{I}_2 + 2\%$   $\text{BiCl}_3$  sample was  $0.59 \text{ mWm}^{-1}\text{K}^{-2}$  at 788 K.

The total thermal conductivity (Figure 3e),  $\kappa_{\text{total}}$ , was calculated from  $D_T \times C_p \times \rho$ , in which  $D_T$  (thermal diffusivity; Supporting Information, Figure S9d) was measured using a laser flash method,  $C_p$  (specific heat; Supporting Information, Figure S9c) was assessed by differential scanning calorimetry (DSC) and  $\rho$  (mass density) was determined geometrically. For the bulk-grain sample,  $\kappa_{\text{total}}$  was  $0.55 \text{ Wm}^{-1}\text{K}^{-1}$  at 363 K, and then decayed to  $0.43 \text{ Wm}^{-1}\text{K}^{-1}$  at 763 K. For the nano  $\text{Bi}_{13}\text{S}_{18}\text{I}_2 + 2\%$   $\text{BiCl}_3$  sample, the in-plane  $\kappa_{\text{total}}$  was  $0.53 \text{ Wm}^{-1}\text{K}^{-1}$  at 313 K, and then decreased to  $0.48 \text{ Wm}^{-1}\text{K}^{-1}$  at 788 K. The cross-plane  $\kappa_{\text{total}}$  of the nano  $\text{Bi}_{13}\text{S}_{18}\text{I}_2 + 2\%$   $\text{BiCl}_3$  sample was even lower.

Combing all the transport properties, the maximum figure of merit,  $zT$  ( $S^2\sigma T \text{K}^{-1}$ ) of 1.0 was achieved at 788 K along the in-plane direction of nano  $\text{Bi}_{13}\text{S}_{18}\text{I}_2 + 2\%$   $\text{BiCl}_3$  sample (Figure 3f). Along the cross-plane direction of this sample,  $zT_{\text{max}}$  was 0.8 at 738 K. The nano-undoped sample showed lower  $zT$  as compared to the doped sample in two directions. For the bulk undoped  $\text{Bi}_{13}\text{S}_{18}\text{I}_2$ , the highest  $zT$  attained was 0.7 at 763 K.

To elucidate the origin of the excellent figure of merit, we have conducted a series of theoretical studies. First, the electronic band structure (Figure 4a) is computed by density

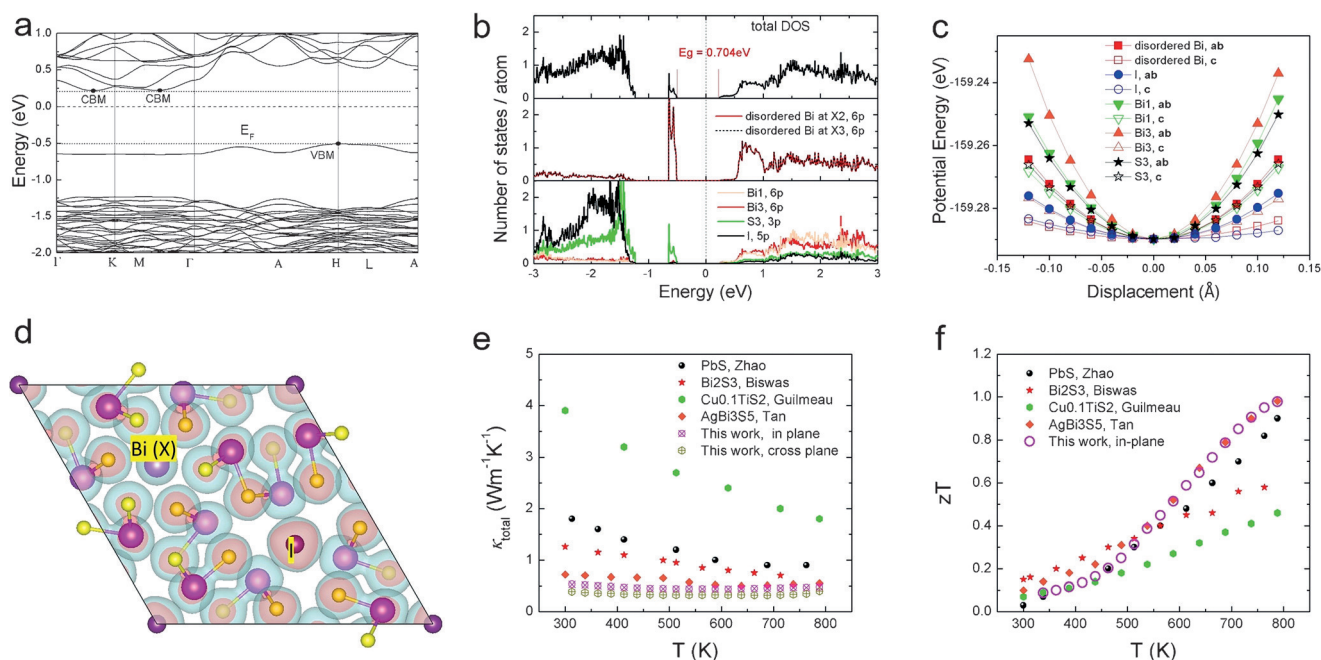


**Figure 4.** a) Electronic band structure, b) density of states, c) potential wells, and d) electron localization function. e), f) Comparison of e)  $\kappa_{\text{total}}$  and f)  $zT$  of our “nano  $\text{Bi}_{13}\text{S}_{18}\text{I}_2 + 2\% \text{BiCl}_3$ ” with those of  $\text{PbS}$ ,<sup>[18]</sup>  $\text{Bi}_2\text{S}_3$ ,<sup>[10a]</sup>  $\text{Cu}_{0.1}\text{TiS}_2$ ,<sup>[10c]</sup> and  $\text{AgBi}_3\text{S}_5$ .<sup>[22]</sup>

functional theory (DFT; see the Supporting Information, Figure S1 for details). As seen from the total density of states (DOS, Figure 4b), the band gap ( $E_g$ ) of  $\text{Bi}_{13}\text{S}_{18}\text{I}_2$  is found to be around 0.70 eV, which is in good agreement with previous optical measurement (0.82 eV).<sup>[14]</sup> Intuitively, the alloying of  $\text{Bi}_2\text{S}_3$  ( $E_g = 1.3$  eV) and  $\text{BiI}_3$  ( $E_g = 1.67$  eV) would yield a compound with  $E_g \approx 1.5$  eV. However, based on the analysis of orbital characters, the Bi(X) atoms with Bi–Bi bond contributed an in-gap state that is located at 0.70 eV below the conduction band minimum (CBM, Figure 4b), resulting in the anomalous shrinkage of the band gap. This  $E_g$  (0.70 eV) is within the proper range ( $6\text{--}10k_B T$ , 0.41–0.69 eV at 800 K) of those of typical mid-temperature thermoelectric materials, such as 0.31 eV of PbTe, 0.41 eV of PbS, and 0.86 eV of SnSe. The narrower band gap (0.70 eV) of  $\text{Bi}_{13}\text{S}_{18}\text{I}_2$  as compared to that of  $\text{Bi}_2\text{S}_3$  (1.3 eV) leads to the more favored activation of charge carrier and concomitant larger electrical conductivity (Supporting Information, Figure S5).

Deeper investigation unveils the double band extrema at the CBM (Figure 4a) that are located between the high symmetry points,  $\Gamma$ –M, and  $\Gamma$ –K, in the Brillouin zone (Supporting Information, Figure S1). They result in a very high valley degeneracy ( $N_v$ ) of 12 in total ( $\text{PbS}$ ,  $N_v = 4$ ,<sup>[18]</sup>  $\text{Bi}_2\text{S}_3$ ,  $N_v = 2$ <sup>[19]</sup>) and a moderate effective mass of electron,  $m^* = 0.30m_0$  ( $\text{PbS}$   $0.39m_0$ ,<sup>[18]</sup>  $\text{Bi}_2\text{S}_3$   $0.40m_0$ <sup>[19]</sup>). This is attributable to the increased symmetry in  $\text{Bi}_{13}\text{S}_{18}\text{I}_2$  (trigonal) as compared to  $\text{Bi}_2\text{S}_3$  (orthorhombic). This high  $N_v$  can also be hinted from the extremely high Seebeck coefficient ( $S = -400 \mu\text{V K}^{-1}$  at 313 K (Figure 3c) with  $n_H = 4.0 \times 10^{18} \text{ cm}^{-3}$  (Figure 3b)) of our nano  $\text{Bi}_{13}\text{S}_{18}\text{I}_2 + 2\% \text{BiCl}_3$  sample as compared to those of other metal sulfide compounds ( $-330 \mu\text{V K}^{-1}$  of  $\text{Bi}_2\text{S}_3$ <sup>[20]</sup> and  $-206 \mu\text{V K}^{-1}$  of  $\text{PbS}$ <sup>[18]</sup>) with the same carrier concentration and similar effective mass. This is because  $S$  at a certain  $n_H$  increases with respect to  $N_v$ <sup>2/3</sup>

and  $m^*$ .<sup>[21]</sup> These features would also favor a high power factor, as  $S^2\sigma$  is proportional to  $N_v$  and inversely proportional to  $m^*$  at a certain carrier concentration.<sup>[21]</sup> Although our nano  $\text{Bi}_{13}\text{S}_{18}\text{I}_2 + 2\% \text{BiCl}_3$  sample had not been optimized in terms of carrier concentration, its peak power factor ( $0.59 \text{ mW m}^{-1} \text{ K}^{-2}$  at 788 K) is comparable to those of the reported metal sulfide thermoelectric compounds ( $0.70 \text{ mW m}^{-1} \text{ K}^{-2}$  for  $\text{AgBi}_3\text{S}_5$ <sup>[22]</sup>) and exceeds that of the optimized  $\text{Bi}_2\text{S}_3$  materials ( $0.47 \text{ mW m}^{-1} \text{ K}^{-2}$ ).<sup>[23]</sup> We expect that through appropriate doping to tune the carrier concentration, an even higher power factor in  $\text{Bi}_{13}\text{S}_{18}\text{I}_2$  may be achieved.

Besides the electrical transport, we have also studied the atomic vibrational properties that may lead to the low thermal conductivity. First, we obtain the potential wells using DFT (Figure 4c). The disordered Bi(X) and I atoms have the flattest potential wells as compared to S and other Bi atoms, especially along the  $c$  direction. This indicates that the Bi(X) and I atoms have much weaker bonding with their neighboring atoms than the other atoms have. Additionally, we have calculated the electron localization function (ELF) as displayed in Figure 4d. It is clearly seen that only the ELF of the Bi(X) and I atoms are spherical, indicating their off-centering instability.<sup>[24]</sup> To directly observe their vibrations, we have conducted ab initio molecular dynamics (AIMD) simulations, and found that the amplitudes of vibration of Bi(X) and I atoms are much larger than other atoms. These data indicate that the Bi(X) and I atoms with relatively weak bonds may lead to low-energy optical modes. These flat optical modes have low group velocities and scatter other phonons much like so-called rattler modes.<sup>[24,25]</sup> As a result, the complex-structured bulk and nano  $\text{Bi}_{13}\text{S}_{18}\text{I}_2$  have exceedingly low  $\kappa_l$  and  $\kappa_{\text{total}}$  as compared to state-of-the-art n-type

metal sulfide thermoelectric materials, such as  $\text{Bi}_2\text{S}_3$ ,<sup>[10a]</sup>  $\text{PbS}$ ,<sup>[18]</sup>  $\text{TiS}_2$ ,<sup>[10c]</sup> and  $\text{AgBi}_3\text{S}_5$ <sup>[22]</sup> (Figure 4e).

According to the aforementioned theoretical analyses,  $\text{Bi}_{13}\text{S}_{18}\text{I}_2$  has featured distinct electronic and phonon structure motifs that may be responsible for its high power factor, low thermal conductivity, and excellent thermoelectric properties. Although the bulk  $\text{Bi}_{13}\text{S}_{18}\text{I}_2$  had not been optimized in terms of doping or nanostructuring, its peak  $zT$  (0.69) is comparable to that of the optimized  $\text{Bi}_2\text{S}_3$  materials (0.72).<sup>[23]</sup> For the nanostructured  $\text{Bi}_{13}\text{S}_{18}\text{I}_2$ , doping, nano-grain boundary scattering (Supporting Information, Figure S12e) and texturization further improve its performance. The  $zT$  of our n-type nano  $\text{Bi}_{13}\text{S}_{18}\text{I}_2 + 2\% \text{BiCl}_3$  sample even outperformed that of n-type  $\text{PbS}$ <sup>[18]</sup> and was nearly identical with that of n-type  $\text{AgBi}_3\text{S}_5$ ,<sup>[22]</sup> at 500–800 K (Figure 4f), without the use of scarce or toxic element. This peak  $zT$  of 1.0 is the highest up to date among n-type, environmentally friendly, and inexpensive thermoelectric metal sulfides.

Last but not least, as a strong candidate for mid temperature (500–800 K) thermoelectrics, our n-type  $\text{Bi}_{13}\text{S}_{18}\text{I}_2$  holds great advantages in terms of toxicity, cost and processability, when compared with state-of-the-art n-type counterparts.  $\text{PbQ}$ <sup>[3,18]</sup> ( $\text{Q} = \text{Te}, \text{Se}, \text{S}$ ) has used large amounts of toxic Pb. In half Heusler compound ( $\text{HfZrNiSn}$ ),<sup>[26]</sup>  $\text{MgSnGe}$ <sup>[27]</sup> and  $\text{In}_4\text{Se}_3$ ,<sup>[28]</sup> the use of expensive Hf ( $\$607\text{kg}^{-1}$ ), Ge ( $\$1250\text{kg}^{-1}$ ), or In ( $\$520\text{kg}^{-1}$ ) impedes their widespread applications, whereas our  $\text{Bi}_{13}\text{S}_{18}\text{I}_2$  consists of very cheap elements (Bi  $\$17\text{kg}^{-1}$ , S  $\$0.09\text{kg}^{-1}$ , and I  $\$27\text{kg}^{-1}$ ).  $\text{SnSe}$  seems to have circumvented all the problems with a  $zT = 2.2$  achieved in n-type single crystals<sup>[4]</sup> and  $zT$  around 1.0 obtained in n-type polycrystalline samples.<sup>[29]</sup> However, the constituent elements (Sn (2.2 ppm), Se (0.05 ppm)) still have much lower abundance than those of  $\text{Bi}_{13}\text{S}_{18}\text{I}_2$  (S (500 ppm), I (0.49 ppm), Bi (0.05 ppm)) in the earth's crust.  $\text{MgSiSn}$  meets the criteria of both low cost and non-toxicity, yet requires high-temperature solid-state processing,<sup>[30]</sup> whereas our low-temperature, solution-phase procedure is energy-saving and time-efficient (only 4 h).

We finally demonstrate the chemical tunability by synthesizing analogous  $\text{Bi}_{19}\text{S}_{27}\text{Br}_3$  nanorods and its nanostructured material (Supporting Information, Figure S11). We foresee that based on proper solution-phase methods, other open-framework compounds derived from canonical binary metal sulfides (selenides), such as  $\text{Sn}_2\text{Bi}_2\text{I}_3$ <sup>[31]</sup> and  $\text{Bi}_{11}\text{Se}_{12}\text{Cl}_9$ ,<sup>[32]</sup> can be synthesized. This strategy can strongly modify the electronic band structure and the phonon transport, thus their thermoelectric properties can be improved. This will enrich the multinary metal sulfides (selenides) as a new family of eco-friendly, cost-efficient, and solution-processable thermoelectric materials.

## Acknowledgements

Y.W. gratefully thanks the support from ACRI and a Herbert L. Stiles Professorship. X.R. thanks the support from DARPA (award number HR0011-15-2-0037). G.J.S. thanks the support from the Department of Energy (award number DE-SC0001299).

## Conflict of interest

The authors declare no conflict of interest.

**Keywords:** band structures · bismuth · iodide · metal sulfides · thermoelectric

**How to cite:** *Angew. Chem. Int. Ed.* **2018**, *57*, 2413–2418  
*Angew. Chem.* **2018**, *130*, 2437–2442

- [1] G. Tan, L.-D. Zhao, M. G. Kanatzidis, *Chem. Rev.* **2016**, *116*, 12123–12149.
- [2] S. I. Kim, K. H. Lee, H. A. Mun, H. S. Kim, S. W. Hwang, J. W. Roh, D. J. Yang, W. H. Shin, X. S. Li, Y. H. Lee, G. J. Snyder, S. W. Kim, *Science* **2015**, *348*, 109–114.
- [3] Y. Pei, X. Shi, A. LaLonde, H. Wang, L. Chen, G. J. Snyder, *Nature* **2011**, *473*, 66–69.
- [4] A. T. Duong, V. Q. Nguyen, G. Duvjir, V. T. Duong, S. Kwon, J. Y. Song, J. K. Lee, J. E. Lee, S. Park, T. Min, J. Lee, J. Kim, S. Cho, *Nat. Commun.* **2016**, *7*, 13713.
- [5] X. Shi, J. Yang, J. R. Salvador, M. Chi, J. Y. Cho, H. Wang, S. Bai, J. Yang, W. Zhang, L. Chen, *J. Am. Chem. Soc.* **2011**, *133*, 7837–7846.
- [6] Y. Zhang, J.-H. Bahk, J. Lee, C. S. Birkel, M. L. Snedaker, D. Liu, H. Zeng, M. Moskovits, A. Shakouri, G. D. Stucky, *Adv. Mater.* **2014**, *26*, 2755–2761.
- [7] J. P. Heremans, V. Jovovic, E. S. Toberer, A. Saramat, K. Kurosaki, A. Charoenphakdee, S. Yamanaka, G. J. Snyder, *Science* **2008**, *321*, 554–557.
- [8] L. Hu, T. Zhu, X. Liu, X. Zhao, *Adv. Funct. Mater.* **2014**, *24*, 5211–5218.
- [9] B. Poudel, Q. Hao, Y. Ma, Y. Lan, A. Minnich, B. Yu, X. Yan, D. Wang, A. Muto, D. Vashaee, X. Chen, J. Liu, M. S. Dresselhaus, G. Chen, Z. Ren, *Science* **2008**, *320*, 634–638.
- [10] a) K. Biswas, L.-D. Zhao, M. G. Kanatzidis, *Adv. Energy Mater.* **2012**, *2*, 634–638; b) Y. He, T. Day, T. Zhang, H. Liu, X. Shi, L. Chen, G. J. Snyder, *Adv. Mater.* **2014**, *26*, 3974–3978; c) E. Guilmeau, Y. Bréard, A. Maignan, *Appl. Phys. Lett.* **2011**, *99*, 052107.
- [11] E. G. Tulskey, J. R. Long, *Chem. Mater.* **2001**, *13*, 1149–1166.
- [12] D. B. Mitzi, L. L. Kosbar, C. E. Murray, M. Copel, A. Afzali, *Nature* **2004**, *428*, 299–303.
- [13] J. Androulakis, S. C. Peter, H. Li, C. D. Malliakas, J. A. Peters, Z. Liu, B. W. Wessels, J.-H. Song, H. Jin, A. J. Freeman, M. G. Kanatzidis, *Adv. Mater.* **2011**, *23*, 4163–4167.
- [14] R. Groom, A. Jacobs, M. Cepeda, R. Drummey, S. E. Lattner, *Chem. Mater.* **2017**, *29*, 3314–3323.
- [15] D.-Y. Chung, T. Hogan, P. Brazis, M. Rocci-Lane, C. Kannerwulf, M. Bastea, C. Uher, M. G. Kanatzidis, *Science* **2000**, *287*, 1024–1027.
- [16] K. Yamana, K. Kihara, T. Matsumoto, *Acta Crystallogr. Sect. B* **1979**, *35*, 147–149.
- [17] X. Shi, J. Yang, S. Bai, J. Yang, H. Wang, M. Chi, J. R. Salvador, W. Zhang, L. Chen, W. Wong-Ng, *Adv. Funct. Mater.* **2010**, *20*, 755–763.
- [18] L.-D. Zhao, S.-H. Lo, J. He, H. Li, K. Biswas, J. Androulakis, C.-I. Wu, T. P. Hogan, D.-Y. Chung, V. P. Dravid, M. G. Kanatzidis, *J. Am. Chem. Soc.* **2011**, *133*, 20476–20487.
- [19] P. Larson, V. A. Greanya, W. C. Tonjes, R. Liu, S. D. Mahanti, C. G. Olson, *Phys. Rev. B* **2002**, *65*, 085108.
- [20] L.-D. Zhao, B.-P. Zhang, W.-S. Liu, H.-L. Zhang, J.-F. Li, *J. Solid State Chem.* **2008**, *181*, 3278–3282.
- [21] Y. Pei, A. D. LaLonde, H. Wang, G. J. Snyder, *Energy Environ. Sci.* **2012**, *5*, 7963–7969.
- [22] G. Tan, S. Hao, J. Zhao, C. Wolverton, M. G. Kanatzidis, *J. Am. Chem. Soc.* **2017**, *139*, 6467–6473.

- [23] Z. Liu, Y. Pei, H. Geng, J. Zhou, X. Meng, W. Cai, W. Liu, J. Sui, *Nano Energy* **2015**, *13*, 554–562.
- [24] M. K. Jana, K. Pal, U. V. Waghmare, K. Biswas, *Angew. Chem. Int. Ed.* **2016**, *55*, 7792–7796; *Angew. Chem.* **2016**, *128*, 7923–7927.
- [25] a) M. Christensen, A. B. Abrahamsen, N. B. Christensen, F. Juranyi, N. H. Andersen, K. Lefmann, J. Andreasson, C. R. H. Bahl, B. B. Iversen, *Nat. Mater.* **2008**, *7*, 811–815; b) M. K. Jana, K. Pal, A. Warankar, P. Mandal, U. V. Waghmare, K. Biswas, *J. Am. Chem. Soc.* **2017**, *139*, 4350–4353.
- [26] S. Chen, K. C. Lukas, W. Liu, C. P. Opeil, G. Chen, Z. Ren, *Adv. Energy Mater.* **2013**, *3*, 1210–1214.
- [27] W. Liu, H. S. Kim, S. Chen, Q. Jie, B. Lv, M. Yao, Z. Ren, C. P. Opeil, S. Wilson, C.-W. Chu, Z. Ren, *Proc. Natl. Acad. Sci. USA* **2015**, *112*, 3269–3274.
- [28] J.-S. Rhyee, K. H. Lee, S. M. Lee, E. Cho, S. I. Kim, E. Lee, Y. S. Kwon, J. H. Shim, G. Kotliar, *Nature* **2009**, *459*, 965–968.
- [29] Q. Zhang, E. K. Chere, J. Sun, F. Cao, K. Dahal, S. Chen, G. Chen, Z. Ren, *Adv. Energy Mater.* **2015**, *5*, 1500360.
- [30] W. Liu, X. Tan, K. Yin, H. Liu, X. Tang, J. Shi, Q. Zhang, C. Uher, *Phys. Rev. Lett.* **2012**, *108*, 166601.
- [31] S. M. Islam, C. D. Malliakas, D. Sarma, D. C. Maloney, C. C. Stoumpos, O. Y. Kontsevoi, A. J. Freeman, M. G. Kanatzidis, *Chem. Mater.* **2016**, *28*, 7332–7343.
- [32] E. K. U. Eggenweiler, V. Kramer, U. Petasch, H. Oppermann, *Z. Kristallogr. Cryst. Mater.* **1999**, *214*, 264.

Manuscript received: January 1, 2018

Accepted manuscript online: January 22, 2018

Version of record online: February 5, 2018